Materials & Design 268 (2026) 116443

Contents lists available at ScienceDirect

Materials & Design

journal homepage: www.elsevier.com/locate/matdes

IN625–CuCrZr multi-material joints by PBF-LB/M: Process–structure–property relationships

Silvia Marola *, Alessandro Carella, Riccardo Casati, Maurizio Vedani

Department of Mechanical Engineering, Politecnico di Milano, Via G. La Masa 1, Milano 20156, Italy

ARTICLE INFO

Keywords:
Laser Powder Bed Fusion
Selective Powder Deposition
Multi-material
Inconel 625
CuCrZr

ABSTRACT

3D-printed multi-material components represent a major advancement in additive manufacturing, allowing the combination of dissimilar materials to achieve tailored properties and functionalities. Recent developments in Laser Powder Bed Fusion (PBF-LB/M) with Selective Powder Deposition modules have enabled the creation of multi-material powder beds, paving the way for complex and functionally graded structures.

This study explores the interfacial features of IN625–CuCrZr components produced by PBF-LB/M, with emphasis on the effects of interface orientation and deposition sequence on microstructure, mechanical, and thermal properties.

Results demonstrate the formation of dense interfaces with continuous metallurgical bonding. The morphology and width of the transition zone vary with both orientation and deposition sequence. EBSD analyses reveal a columnar-to-equiaxed grain transition when moving from IN625 to CuCrZr. Mechanical tests, especially in-situ SEM tensile tests, suggest that joint strength and crack development strongly depend on interface orientation and loading direction. Laser flash analysis highlights enhanced thermal diffusivity in CuCrZr–IN625 joints, exceeding that of monolithic IN625, thus suggesting potential for high-performance applications.

These findings clarify deposition-sequence effects on interfacial bonding, intermixing, defects, and performance in IN625/CuCrZr architectures.

1. Introduction

In the last 20 years, Additive Manufacturing (AM) has evolved into a key enabling technology for the production of metallic components, offering design freedom, reduced production times, and the ability to tailor material properties [1,2]. One of the most recent and promising evolutions of AM is represented by Multi-Material Additive Manufacturing (MMAM), which enables the combination of dissimilar alloys within a single component to deliver application-specific functionalities or to produce Functionally Graded Materials (FGM) [3–8]. This approach is particularly attractive for applications in aerospace, energy, and biomedical sectors, where the simultaneous demand for high strength, thermal conductivity, and corrosion resistance make multi-material solutions especially advantageous.

Among the various AM techniques, Directed Energy Deposition (DED) and Laser Powder Bed Fusion of metals (PBF-LB/M) are currently regarded as the most technologically mature, holding the highest potential for industrial implementation of MMAM [3,6,9,10]. Within this framework, Selective Powder Deposition (SPD) strategies represent a cutting-edge evolution of PBF-LB/M, as they allow spatial alloy changes to be treated as a design variable, enabling targeted property placement within a single component [11,12].

Despite these advances, a major challenge in MMAM remains the control of interfaces between dissimilar alloys. Interfacial bonding mechanisms, defect formation, and property gradients are strongly influenced by factors such as interface orientation and deposition sequence, yet systematic studies on these aspects remain limited [13].

Among the multi-material pairings currently receiving increasing attention, those combining structural performance with efficient heat transfer capability, such as steel/copper or nickel/copper systems, are particularly relevant. These combinations are attractive for advanced engineering applications, including tooling, heat exchangers, and energy conversion devices, where high mechanical strength and superior thermal conductivity must coexist [14–18]. Despite the potentially attractive properties of steel/copper multi-materials, their coupling remains challenging due to differences in physical and metallurgical characteristics. Cracks frequently nucleate and propagate along the interface, predominantly on the steel side, thereby compromising joint

* Corresponding author.
E-mail address: silvia.marola@polimi.it (S. Marola).

https://doi.org/10.1016/j.matdes.2026.116443
Received 19 November 2025; Received in revised form 19 May 2026; Accepted 16 June 2026
Available online 17 June 2026

integrity [3,13,19]. The origin of such defects arises from a complex interplay of factors, including: (i) the Fe–Cu miscibility gap, which promotes phase separation and compositional inhomogeneities; (ii) the thermophysical mismatch between steel and copper generating high residual stresses; (iii) disparities in solidification behavior that foster hot cracking; and (iv) the high thermal conductivity of copper, which reduces the effective energy input during laser processing toward the steel layer, hindering proper melting and metallurgical bonding. Together, these mechanisms limit the processability and performance of steel/copper components, highlighting the need for careful optimization of processing strategies.

Nickel–copper systems offer a promising alternative, since Ni-based superalloys provide excellent high-temperature strength, thermal stability, and chemical resistance, while copper alloys contribute with high thermal conductivity, making these pairings suitable for applications requiring excellent combinations of functional and mechanical properties [10,18,20–22]. Unlike Fe–Cu systems, Ni and Cu both share an FCC lattice, feature closer values of the coefficient of thermal expansion (CTE), and are fully miscible in both liquid and solid states, facilitating the formation of sound, defect-free interfaces and reducing residual stresses [23,24].

Despite the maturity of single-material processing, fabricating the two alloys simultaneously remains challenging. Minor variations in composition or thermal history can induce undesired effects, including sharp property gradients, residual stresses, and brittle intermetallic formation, potentially compromising joint integrity [22,25–27]. Studies on IN718–Cu and IN718–CuCrZr have shown that optimized parameters, deposition strategies, and layer orientations can produce dense interfaces with gradual hardness transitions and strong metallurgical bonding driven by mechanisms such as Marangoni convection, remelting, and interdiffusion [17,28–33]. Compared to IN718-based systems, IN625–CuCrZr offers greater weldability thanks to its composition, which limits intermetallic formation and cracking [20,22]. Proper control of laser power and preheating enhances Ni–Cu interdiffusion and facilitates the development of interlocking lamellae improving mechanical cohesion, while reduced energy in upper layers prevents coarsening and keyhole defects, yielding a uniform, defect-free microstructure [20].

The deposition sequence, namely the order of Cu- and Ni-alloy deposition, and applied laser power critically influence melt pool composition, solidification pathway, intermetallic formation, and the overall mechanical performance of the joint. However, under optimized processing conditions, tensile tests indicate that fracture occurs predominantly within the softer CuCrZr alloy rather than at the interface, confirming the effectiveness of the metallurgical bond [10,20,21].

Nevertheless, recent studies indicate that the behavior of IN625–CuCrZr systems is more complex than previously anticipated. Alloying elements in IN625 induce a liquid-phase miscibility gap, resulting in Ni-rich and Cu-rich domains during solidification, which transform into two distinct FCC solid solutions and, under certain conditions, can induce precipitation of intermetallic phases such as Laves and P-phase [22,24]. These phenomena can beneficially promote fine equiaxed grain formation; however, they may also contribute to cracking when local compositional variations caused by dilution reach critical levels. This crack susceptibility is linked to the extended solidification range, which favors defect initiation in Cu-rich liquid within the Ni-rich mushy zone during the final stages of solidification, driven by shrinkage and thermal stresses from rapid cooling [24].

Overall, these findings highlight the critical role of a well-controlled combination of laser parameters and deposition strategy in achieving reliable, high-performance IN625–CuCrZr multi-material components suitable for demanding applications such as aerospace propulsion systems, where structural integrity and efficient heat dissipation must coexist.

This study provides a systematic and comprehensive investigation of the interfacial bonding mechanisms in IN625–CuCrZr multi-material components fabricated via PBF-LB/M equipped with a selective powder deposition (SPD) recoating system. By systematically varying interface orientation and material deposition sequence, this work elucidates how these parameters govern interface width, grain morphology, and defect formation, ultimately affecting the mechanical and thermal performance of the bi-metallic components.

Unlike previous studies, which have primarily addressed isolated aspects of the interface, this work offers an integrated, multi-scale analysis that directly links microstructural evolution to the resulting mechanical and thermal behavior. A comprehensive experimental framework, combining optical microscopy, Field Emission Scanning Electron Microscope (FE-SEM) with Energy Dispersive X-ray Spectroscopy (EDS) and Electron Back-Scattered Diffraction (EBSD) analyses, *in-situ* tensile testing, and thermal diffusivity measurements, was employed to uncover the process–structure–property relationships that dictate bonding quality and functional performance in Ni–Cu multi-material systems. The findings provide additional insight into how deposition sequence and interface orientation affect metallurgical bonding, elemental intermixing, defect formation, and functional performance in IN625–CuCrZr multi-material components. This systematic approach helps identify experimentally supported considerations for controlling interfacial architectures through deposition strategy and interface orientation.

2. Materials and methods

Specimens were printed via PBF-LB/M using an Aconity MIDI + system equipped with an Aerosint SPD recoater under argon, employing gas-atomized IN625 (Carpenter Additive, CT POWDERRANGE 625F) and CuCrZr (Eckart AMsphere) powders, whose nominal compositions are reported in Table 1. All samples were produced using the parameter sets optimized for each mono-material alloy. CuCrZr alloy was processed with a laser power of 500 W at a scan rate of 800 mm·s^{-1}, while IN625 alloy was processed at 160 W and at 750 mm·s^{-1}. For both alloys, the hatch spacing and layer thickness were selected at 80 µm and 40 µm, respectively. The scanning strategy included a 67° rotation between successive layers. The system operated with an IR laser ($\lambda = 1070$ nm) featuring a spot size of 80 µm.

For specimens with a vertical interface, the IN625 section was scanned first in each layer, followed by the CuCrZr portion. For all the samples, the optimized mono-material parameters were applied without introducing correction factors or specific adjustments at the interface.

The experimental campaign included twelve specimens (Fig. 1a): six 12 × 12 × 12 mm cubes for metallography, microhardness, and thermal diffusivity measurements, and six 48 × 12 × 12 mm bars for dog-bone micro-tensile specimens (gauge length $L_0 = 15$ mm, width b = 5 mm, thickness $t \approx 1.2$ mm, Fig. 1b), which were cut to their final shape using wire electrical discharge machining (W-EDM). Prior to tensile testing, the EDM-affected surface layer was removed using abrasive paper to ensure artifact-free surfaces. Three joint configurations were investigated for the multi-material samples: vertical interface (bar sample on the right of Fig. 1a), horizontal interface with IN625 above CuCrZr (bar sample at center of Fig. 1a), and horizontal interface with CuCrZr above IN625 (bar sample on the left of Fig. 1a). Specimens for mechanical testing were extracted either perpendicular (xz plane) or parallel (xy plane) to the build plate to assess build orientation effects. Mono-material reference data were assessed using specimens taken from volumes of homogeneous materials, extracted far from the interface regions, at a minimum distance of 2.5 mm, to avoid compositional gradients. A schematic representation of the specimen extraction strategy for the tensile tests is provided in Fig. 1c.

The different multi-material samples have been identified by a first letter referred to the interface orientation, perpendicular (V) or parallel (H) to build plate, by a subscript indicating the plane from which tensile specimens have been cut, xy or xz, and by the chemical symbol (Ni or Cu) for the alloy placed on top of samples with horizontal interface. For

Table 1
Nominal chemical composition (in wt.%) of IN625 and CuCrZr alloys.

	Cr	Mo	Nb	Fe	Zr	Si	C	O	Ni	Cu
IN625	20.0–23.0	8.0–10.0	3.15–4.15	5.0	–	–	0.1	0.03	Bal.	–
CuCrZr	0.50–1.20	–	–	0.08	0.03–0.30	0.10	–	–	–	Bal.

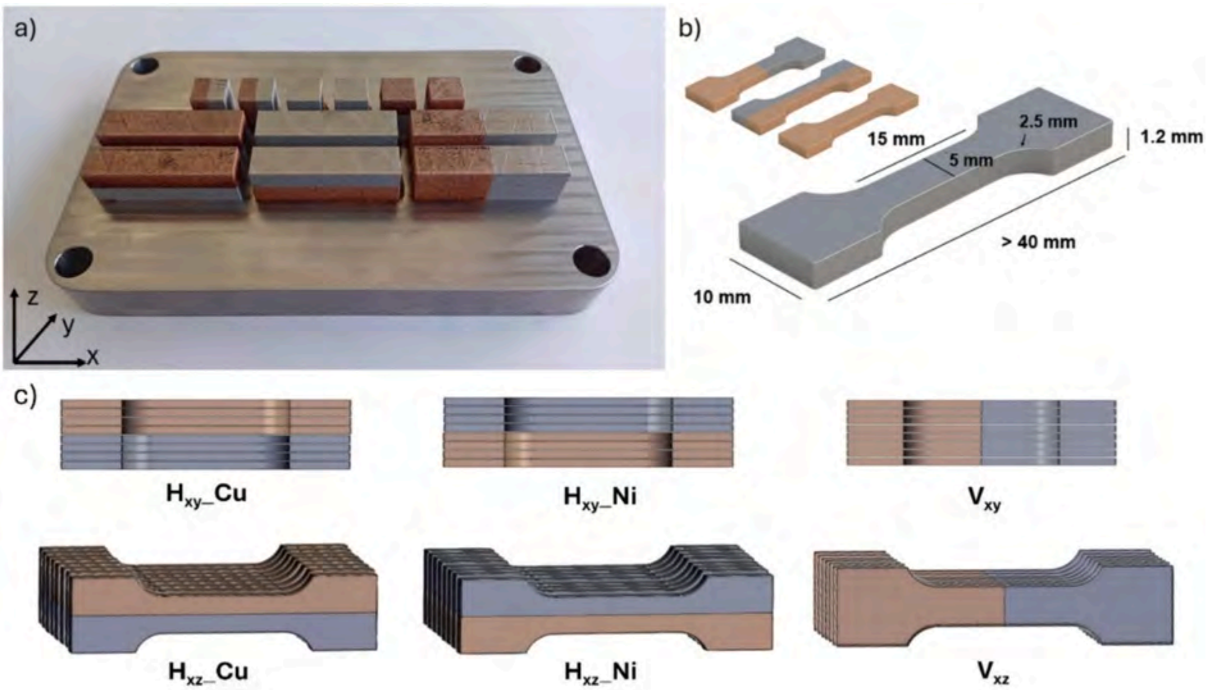

Fig. 1. Bi-metallic IN625-CuCrZr samples (a) and schematic representation of the dog-bone specimens in the four possible material configurations. One specimen configuration has been enlarged to show the size of the dog-bone specimens (b). A schematic illustration of the extraction strategy and build orientation of the dog-bone specimens is shown in (c).

mono-material specimens extracted from the bars, the same nomenclature was adopted; additionally, the material constituting the entire dog-bone specimen is indicated in parentheses. In summary, sample IDs, interface types, and deposition sequences are listed in Table 2.

Standard metallographic procedures, involving sequential grinding with decreasing grit sizes followed by polishing with diamond suspensions down to 1 μm, were carried out to prepare the samples for microstructural analysis. Samples intended for SEM analyses received an additional polishing step using colloidal silica (SiO_2). The same preparation was applied to tensile specimens for *in-situ* SEM tensile testing.

Porosity was quantified by optical microscopy (Nikon Eclipse LV150NL with DS-U3 camera, NIS Elements v4.60) using panoramic images (25X) stitched from multiple micrographs. For each sample a total of 10 cross-sections were analyzed to determine the reported density. The sections were obtained from different specimens and included both xy (parallel to the build plane) and xz (along the build direction) orientations. Images were converted to grayscale, binarized in ImageJ, and corrected manually for artifacts to estimate areal porosity.

Microstructural analysis was performed using a FE-SEM (Zeiss Sigma 500) equipped with EDS (Oxford Instruments Ultim Max) and EBSD (Oxford Instruments C-Nano) detectors. FE-SEM was employed to examine microstructure and interfaces; EDS line scans (along a length of 2000 μm) across interfaces allowed identifying elemental gradients and transition zone width, while EBSD was used to map grain orientation and size, with phase discrimination supported by EDS to differentiate FCC γ-Ni and α-Cu phases.

Microhardness was measured with a microindenter (Future Tech FM-700) following the ISO 6507–1:2023, applying 100 g_f for 10 s. Profiles perpendicular to the interface were sampled every 500 μm, and ∼ 10 indents were measured within single-material regions to attain averaged values. The beginning and the end of the transition zone were determined from the hardness profile at points where the hardness deviated by 10 % from the baseline values of the adjacent homogeneous alloy.

Thermal diffusivity was measured by laser flash analysis (LINSEIS LFA 1000) on three 10 × 10 × 2 mm specimens for each interface configuration, including the two mono-materials and bi-materials

Table 2
Summary of the sample ID, interface type and deposition sequence of the samples (for microstructure analyses and for tensile testing) investigated.

Sample ID Microstructure	**Tensile**	Interface type	Deposition sequence
V_{xz},	V_{xy}, V_{xz}	Vertical	IN625 | CuCrZr
H_{xz}_Ni	H_{xy}_Ni (IN625), H_{xy}_Ni (CuCrZr), H_{xz}_Ni	Horizontal	IN625 on CuCrZr
H_{xz}_Cu	H_{xy}_Cu (IN625), H_{xy}_Cu (CuCrZr), H_{xz}_Cu	Horizontal	CuCrZr on IN625

containing the transition zone. The specimens for testing were extracted by sectioning the samples with the vertical interface along the yz plane, while those with the horizontal interface were cut along the xy plane. A vacuum level below 10^{-2} mbar was kept in the chamber during the LFA tests.

Micro-tensile tests were conducted using a Kammrath & Weiss electromechanical module (maximum load 5 kN) under displacement control ($\dot{\varepsilon} \approx 1 \times 10^{-4}$ s^{-1}, ISO 6892-1, A1/A2), using an external extensometer placed on the gauge length of specimens. The largest number of tests were performed *ex-situ*, to evaluate tensile performance and fracture mode. Additional *in-situ* SEM tests were performed to investigate the damage evolution during tensile straining. For each material and interface condition, three samples were tested. Dog-bone specimens for *ex-situ* testing were ground to P600 grit to remove W-EDM-affected layers and reduce their thickness to keep the fracture load within the range of the load-cell (the thickness had to be reduced to 0.8 mm for mono-material IN625 specimens).

3. Results and discussion

3.1. Microstructure of alloys and interface characterization

3.1.1. Mono-materials characterization

Fig. 2 presents the micrographs of IN625 and CuCrZr regions taken far from the interface, illustrating the processability of each single material under the applied processing parameters. The mono-materials achieved relative densities of approximately 99.6 % for IN625 and 99.0 % for CuCrZr. The IN625 alloy exhibits a consistently dense microstructure with uniformly distributed fine gas pores, having an average diameter of about 6 μm, whereas the CuCrZr alloy shows a higher fraction of larger, rounded porosities. The different defect morphologies observed in the IN625 and CuCrZr regions can be related to the different laser–material interaction and thermal behavior of the two alloys. The finer porosity observed in IN625 is consistent with a more stable melt-pool condition [34], while the larger pores observed in CuCrZr can be associated with the higher processing difficulty of Cu-based alloys, arising from their high reflectivity/low absorptivity under IR laser radiation and high thermal conductivity [35]. Hardness measurements reveal values of 334 ± 11 $HV_{0.1}$ for IN625 and 132 ± 21 $HV_{0.1}$ for CuCrZr. Notably, the latter alloy showed a significant variation in hardness along the build direction, decreasing from 154 ± 3 $HV_{0.1}$ near the building plate to 115 ± 7 $HV_{0.1}$ at top of the sample (Fig. S1 in Supplementary Information). The observed gradient is consistent with the occurrence of a progressive aging in the CuCrZr alloy due to the thermal cycles induced by the layer-by-layer deposition, promoting the precipitation of strengthening phases.

Overall, these findings show that the hardness values measured for both IN625 and CuCrZr alloys are in good agreement with those reported in the literature for similarly processed systems [36,37], supporting the adequacy of the selected processing parameters.

3.1.2. Interfaces characterization

Representative micrographs focused on the interface region of the investigated multi-material configurations are shown in Fig. 3. In Fig. 3a–c low-magnification views of almost the entire cross-section of the specimens are reported, showing the distribution of defects both at the interface and within the mono-material regions. In the multi-material samples, localized porosity accumulation was mainly observed in the CuCrZr regions close to IN625 or to the steel base plate. In these cases, the lower thermal conductivity of IN625 and steel compared with CuCrZr may reduce heat extraction from the CuCrZr melt pool, promote local heat accumulation, and further disturb melt-pool stability, contributing to the formation of larger pores.

Besides interface-related issues, printing-related defects can also be identified. In particular, the H_{xz}_Ni sample (Fig. 3b) exhibited localized accumulations of lack-of-fusion defects within a limited number of layers, as pointed out by the arrow in the image, suggesting the occurrence of an occasional perturbation of the process. Similarly, the CuCrZr mono-material regions show porosities locally clustered in specific areas, suggesting that occasional process instabilities may have caused non-ideal solidification conditions. The observed defects are most plausibly attributable to localized irregularities in powder deposition occurring during the recoating of specific layers. This effect can be more pronounced when using a multi-material recoating system, where process complexity increases. Typical challenges include local inhomogeneities in powder distribution, slight misalignment between deposition modules, and transient interruptions in powder feeding. Such events may affect individual layers, leading to isolated lack-of-fusion defects, while not substantially compromising the general results collected in the present investigation. The consistently high average density measured across multiple cross-sections supports the conclusion that these defects are sporadic and do not reflect a general lack of process stability.

From Fig. 3a–c, it is evident that all IN625–CuCrZr multi-material configurations exhibit predominantly dense and continuous metallurgical bonding at the interface. However, it is worth noting that the extension and quality of the interface strongly depend on the sample orientation and the deposition sequence of the two materials. V_{xz} samples show small pores mostly located on the CuCrZr side close to the interface, with a moderate degree of intermixing at the joint boundary (Fig. 3a, d, and g). H_{xz}_Ni samples (IN625-on-CuCrZr) display a sharp interface free of macroscopic defects with no visible intermixing (Fig. 3b, e, and h), while H_{xz}_Cu (CuCrZr-on-IN625) samples exhibit a broad intermixing region and the highest defectivity, with cracks and pores concentrated in the Cu-rich region, along with a more diffuse interface boundary (Fig. 3c, f, and i).

In the H_{xz}_Cu samples, the pores located near the interface are mostly spherical, consistent with a keyhole-origin mechanism. Cracks were

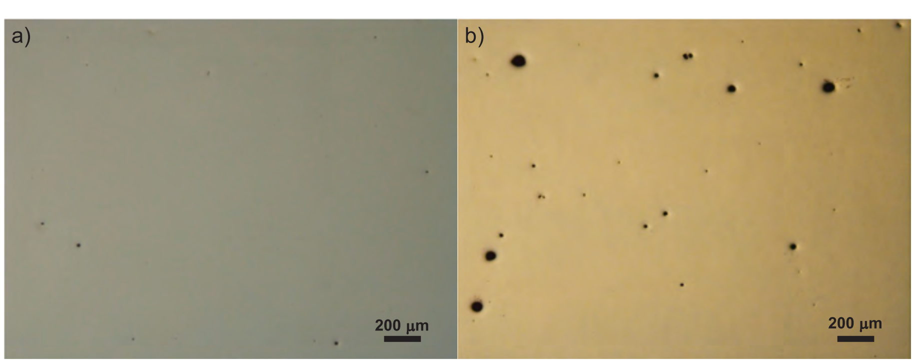

Fig. 2. Optical micrographs of the IN625 (a) and CuCrZr (b) alloys acquired far from the interface, illustrating the main defects of the individual materials under the applied processing parameters.

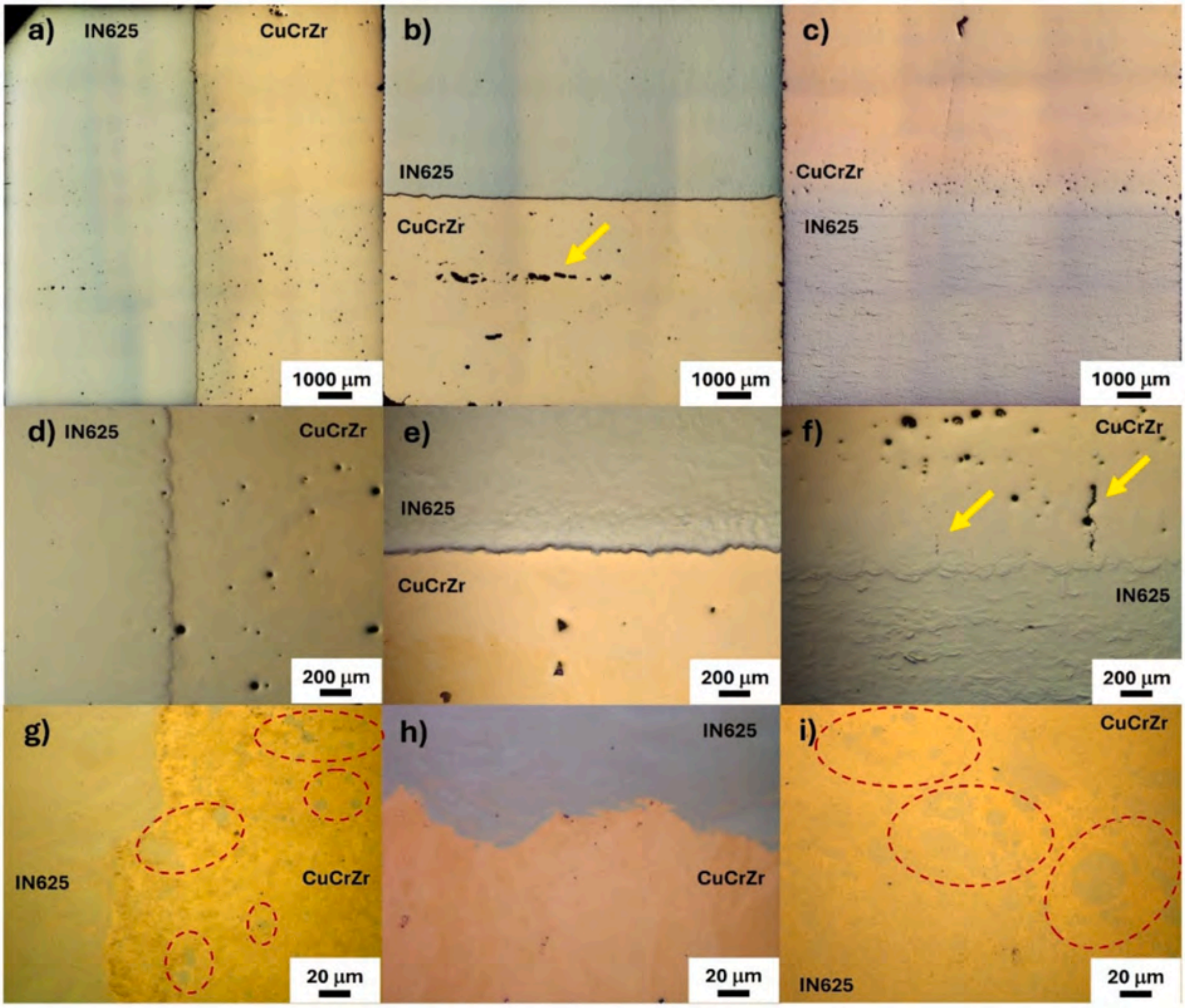

Fig. 3. Optical micrographs of the three interface configurations taken at different magnifications: (a, d, and g) vertical interface (V), (b, e, and h) horizontal interface with IN625 deposited on CuCrZr (H_Ni), (c, f, and i) horizontal interface with CuCrZr deposited on IN625 (H_Cu). The yellow arrows highlight defects due to process perturbation in (b) and cracks along the interface in (f). The red dashed circles in (g) and (i) mark the Ni-rich/Cu-rich domains in the Ni–Cu intermixing area at the interface. (For interpretation of the references to colour in this figure legend, the reader is referred to the web version of this article.)

invariably found within the intermixing region, spanning a few hundred micrometers in length. Detailed EDS analyses revealed that these cracks occur in regions with average Cu content ranging from approximately 50 ± 12 wt% at the Cu-rich crack tip to 24 ± 4 wt% at the Cu-poor crack tip, confirming their localization within the mixed Cu–Ni zone.

In micrographs reported in Fig. 3g and 3i, red dashed circles highlight the presence of small-size islands showing a different color contrast, which correspond to Ni-enriched areas embedded in the Cu-rich domain. Such features have already been observed by Özsoy et al. [24] for the CuCrZr/IN625 system. Their results indicate that cracking in this material combination cannot be explained solely on the basis of the binary Ni–Cu phase diagram, since the critical mechanism arises from the multicomponent interaction between Cu and the main alloying elements of IN625, particularly Cr, Fe, and Mo. These interactions promote liquid-phase immiscibility at high temperature, leading to the separation of the melt into Cu-rich and Ni-rich liquid regions. During cooling, the Ni-rich liquid solidifies first, whereas Cu-rich liquid films can persist over an extended solidification interval along interdendritic or intergranular regions. The presence of these residual Cu-rich liquid films reduces feeding capability during the final stages of solidification and promotes terminal solidification cracking under the thermal stresses generated during PBF-LB/M. This mechanism is consistent with the crack localization observed in the present work within the mixed Cu–Ni region, where EDS measurements revealed Cu contents ranging from approximately 50 ± 12 wt% to 24 ± 4 wt%. The higher cracking susceptibility of H_{xz}_Cu can therefore be attributed to its broader transition zone, which increases the volume of material crossing the crack-sensitive compositional range. Conversely, the sharper interface in H_{xz}_Ni limits this critical mixed region and reduces cracking susceptibility. Within the resolution of the SEM-EDS and EBSD analyses performed in this work, no continuous secondary-phase layer or clearly detectable precipitation band was observed at the IN625–CuCrZr interface. Therefore, the present discussion focuses on compositional mixing, grain refinement, defect formation, and crack localization. Possible nanoscale precipitation or intermetallic formation induced by local interdiffusion cannot be excluded, but its confirmation would require dedicated high-resolution analyses, such as TEM, APT, or synchrotron-based phase characterization, which are beyond the scope of the present study.

Fig. 4 presents the results of the combined EBSD and EDS analyses for the different interface configurations. The inverse pole figure (IPF) maps of the three analyzed samples reveal that, far from the interface, both IN625 and CuCrZr display the typical microstructure of materials produced by PBF-LB/M, consisting of coarse columnar grains having equivalent circle diameter (ECD) of approximately 35 μm predominantly elongated along the building direction (BD, vertical in the

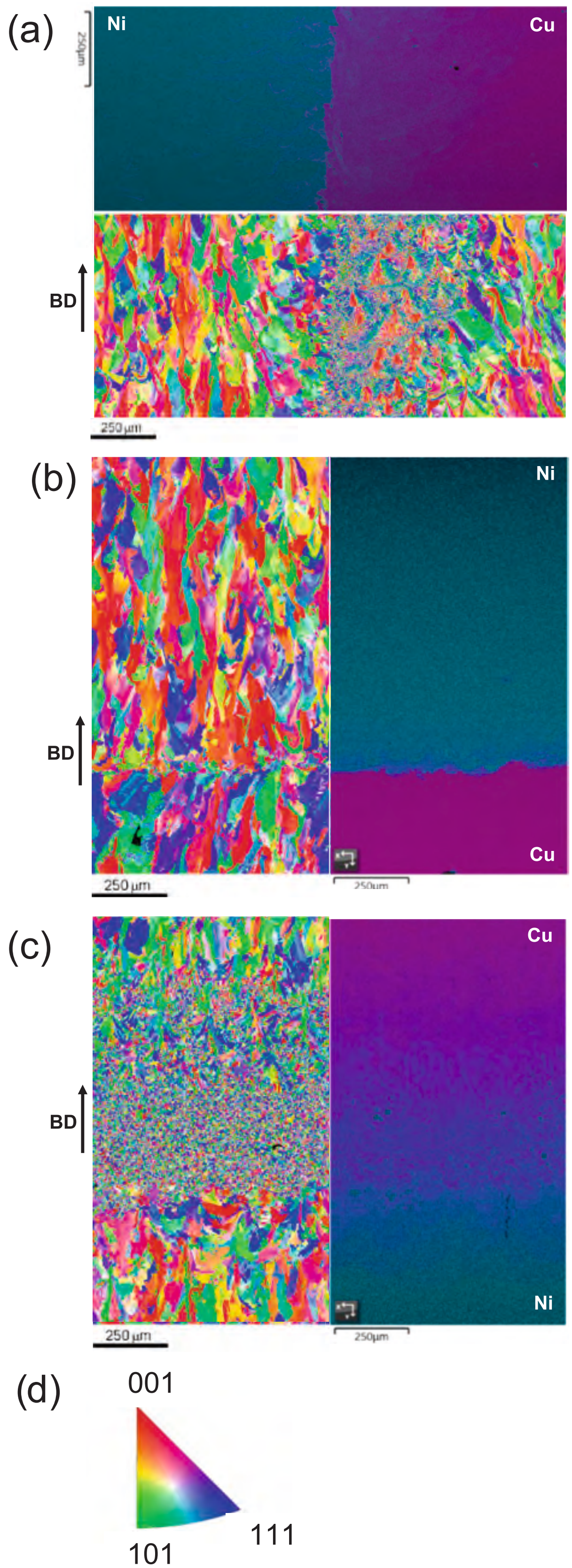

Fig. 4. SEM–EDS maps and IPF maps for the three interface configurations. (a) Vertical (V), (b) horizontal with IN625 deposited on CuCrZr (H_Ni), (c) horizontal with CuCrZr deposited on IN625 (H_Cu). The color key for the IPF maps is reported in (d).

figures).

Although epitaxial growth across dissimilar-material interfaces can strongly affect interfacial strength, the IPF maps reported in Fig. 4 do not indicate continuous epitaxial growth across the IN625/CuCrZr interface. In all configurations, the interface is instead characterized by the interruption of columnar growth and by local grain refinement, with fine equiaxed grains forming within the intermixing zone. This suggests that, in the present system, the interfacial response is governed mainly by the extent of alloy mixing, defect formation and crack-susceptible compositional regions, rather than by epitaxial growth competition across the interface.

In the IN625 region of the V_{xz} sample (Fig. 4a) a coarser microstructure is retained even near the interface. The transition zone therefore extends almost entirely into the copper-alloy domain and is characterized by extremely fine (ECD ≈ 6 μm), equiaxed grains, reflecting rapid cooling and local composition changes within the miscibility gap. Moving further into the Cu-rich region, columnar growth is progressively re-established. EDS line profiles displayed in Fig. 5, acquired in a different region and covering a larger portion of the specimen than that shown in Fig. 4, provide additional information about the full extension of elemental dilution induced by the laser processing. The profile referred to the V_{xz} sample (Fig. 5a) highlights a sharp variation in Cu and Ni content when crossing the interface, with limited short-range diffusion on both sides of the interface.

The H_{xz}_Ni sample (Fig. 4b) where CuCrZr alloy was deposited first, retains coarse grains up to the interface, where some refinement occurs due to alloy mixing (ECD ≈ 27 μm). However, this effect appears limited likely because of the rapid cooling imposed by both the reduced laser power required to print IN625 and the high thermal conductivity of the copper alloy. As a result, the H_{xz}_Ni sample exhibits a comparatively narrower, almost negligible transition zone with tiny equiaxed grains. Grains in the upper half of the joint quickly revert to a coarse columnar morphology aligned with the main thermal gradient, making the horizontal interface of sample H_{xz}_Ni the sharpest among the investigated configurations.

From Fig. 5b, it can be inferred that all the main elements diffuse across the interface over a short distance, supporting the assumption that the Cu-content may lie outside the crack-prone compositional range over extended volumes, thereby mitigating the hot-cracking susceptibility.

Conversely, the H_{xz}_Cu sample (Fig. 4c and Fig. 5c) exhibits extensive remelting and alloy mixing owing to the higher energy density used for processing of the CuCrZr alloy in the upper layers. This higher heat input generates a broad interfacial region that spans the crack-prone compositional range over a wider distance, in agreement with the pronounced cracking susceptibility observed in Fig. 3f. Microstructural observations (Fig. 4c and Fig. S2 in Supplementary Information) indicate that cracks preferentially propagate in regions where Cu-rich liquid films are trapped between Ni-rich columnar grains. The fine equiaxed-grain zone (ECD ≈ 8 μm) shown by IPF map in Fig. 4c exhibits a wide extension, which is consistent with the significant compositional shift reported in the EDS line profile in Fig. 5c.

Hardness profiles displayed in Fig. 6 are consistent with the extension of the transition zone determined by SEM-EDS and EBSD analyses. Since IN625 is harder than CuCrZr, the hardness variation across the interface was used as a complementary indicator to assess the width of the intermixing region. In this sense, the sharp hardness transition observed in H_{xz}_Ni (Fig. 6b) agrees with the sharp interface, limited alloy mixing, and narrow transition zone observed in the corresponding microstructural and compositional maps. Conversely, the broader hardness transitions measured in V_{xz} (Fig. 6a) and H_{xz}_Cu (Fig. 6c) are consistent with the wider intermixing regions revealed by SEM-EDS and with the refined equiaxed grains observed by EBSD in the transition zone.

In V_{xz} and H_{xz}_Cu, the Cu-rich transition zone exhibits a slight hardness increase of approximately 25 $HV_{0.1}$ compared with the CuCrZr

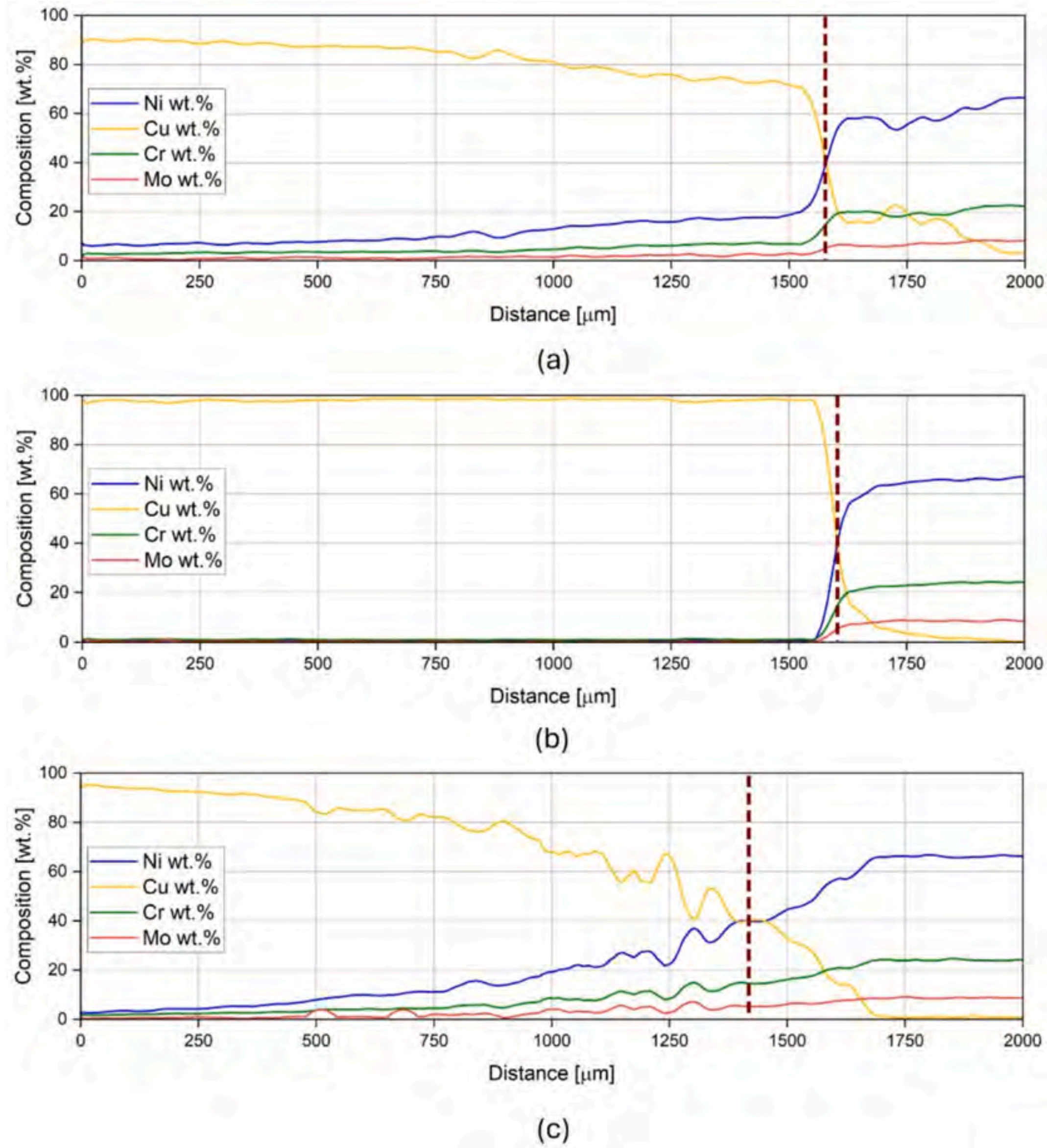

Fig. 5. Elemental composition profiles across the interfaces of (a) Vertical (V_{xz}), (b) horizontal with IN625 deposited on CuCrZr (H_{xz}_Ni), (c) horizontal with CuCrZr deposited on IN625 (H_{xz}_Cu). The dashed vertical lines show the assumed position of the geometrical interface.

mono-material region. This increase can be attributed to the combined effect of grain refinement and local compositional changes induced by partial mixing with IN625. Indeed, liquid-phase separation in the CuCrZr/IN625 system can promote the formation of Cu-rich and Ni-rich regions, which solidify as compositionally distinct solid-solution domains. The partial incorporation of Ni and other IN625 alloying elements into the Cu-rich transition zone may therefore provide a solid-solution strengthening contribution, while the refined equiaxed grain structure further contributes to the measured hardness increase. Therefore, the hardness profiles do not only reflect the intrinsic hardness difference between the two base alloys, but also provide additional evidence of the extent of microstructural and chemical mixing at the interface.

Further hardness tests performed along the building direction in the CuCrZr mono-material region revealed no clear monotonic hardness variation in either H_{xz}_Ni or H_{xz}_Cu. This suggests that processing-induced aging effects were not dominant under the investigated conditions. In H_{xz}_Ni, this behavior is likely related to the lower volumetric energy density used for processing IN625, which limits heat transfer toward the previously deposited CuCrZr layers. In H_{xz}_Cu, it can be associated with the limited number of deposited layers, which reduces the overall thermal exposure required to promote aging phenomena.

The combined analysis of the collected results confirms that the extent of the intermixing zone and, consequently, the interface width, varies as a function of interface orientation and deposition sequence. IPF maps show that the columnar–equiaxed–columnar transition changes significantly among different configurations, with equiaxed grains dominating the transition zone, where alloy mixing is most pronounced. EDS profiles combined with hardness measurements indicate that, in samples with a horizontal interface, the interfacial region varies from approximately 350 μm (H_{xz}_Ni) to nearly 2 mm (H_{xz}_Cu) simply by reversing the deposition order. The vertical interface configuration exhibits an intermediate extension of about 1 mm. These findings further suggest that more compact interfaces can mitigate cracking by reducing the extent of the 20–40 wt% Cu region identified as critical for crack formation with the present experiments and confirmed by literature results [24].

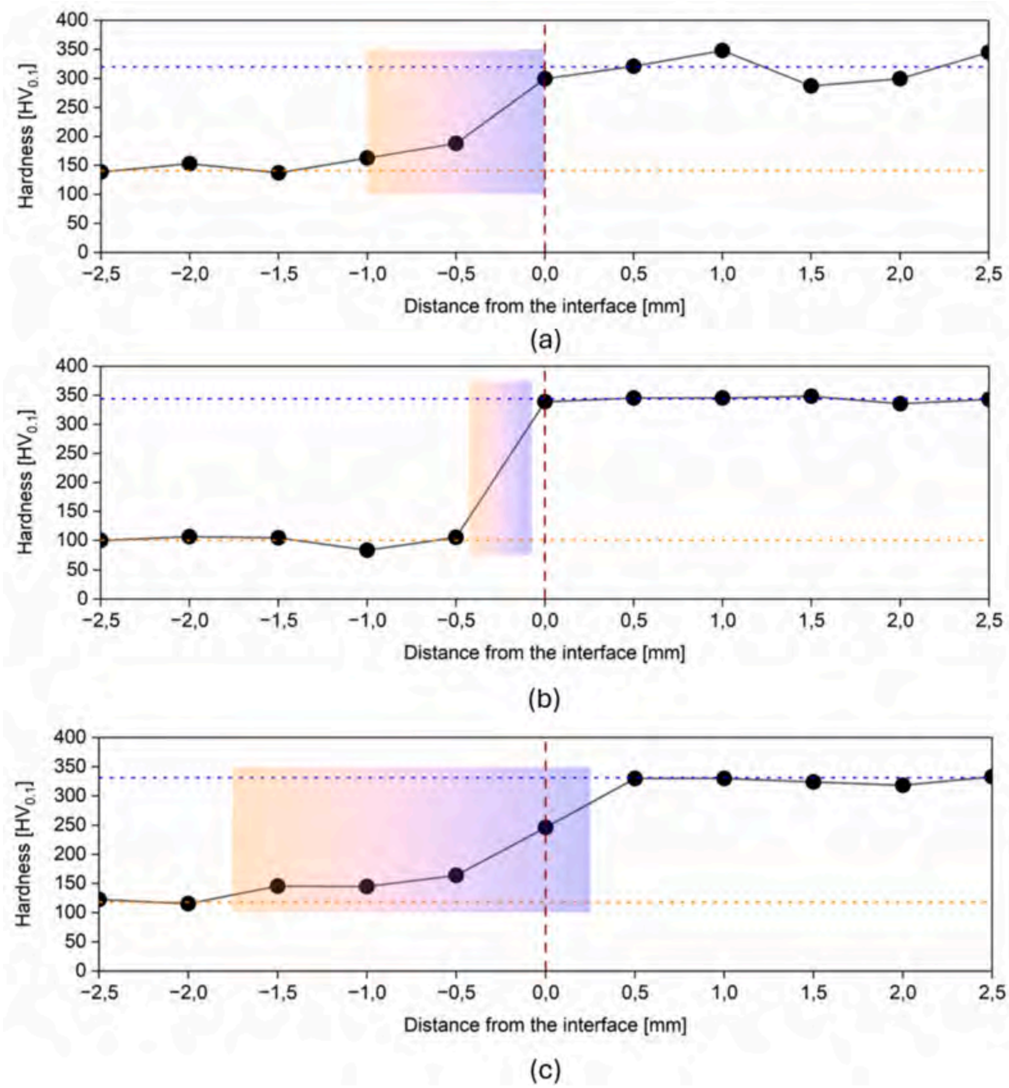

Fig. 6. Hardness profiles across the interface for (a) Vertical (V_{xz}), (b) horizontal with IN625 deposited on CuCrZr (H_{xz}_Ni), (c) horizontal with CuCrZr deposited on IN625 (H_{xz}_Cu). The orange and blue dotted lines represent the average hardness of the mono-material regions, while the dashed red line represents the assumed position of the geometrical interface. The colored boxes mark the extension of the intermixing zones identified through these measurements. (For interpretation of the references to colour in this figure legend, the reader is referred to the web version of this article.)

Table 3
Tensile properties of the materials investigated: 0.2 % yield strength (YS), ultimate tensile strength (UTS), and elongation at fracture (e_{max}).

Sample ID	Deposition sequence & Specimen details		YS [MPa]	UTS [MPa]	e_{max} [%]
H_{xy}_Cu (CuCrZr)	CuCrZr mono-material		259 ± 8	310 ± 10	18 ± 7
H_{xy}_Cu (IN625)	IN625 mono-material		850 ± 20	1209 ± 2	38 ± 1
H_{xy}_Ni (IN625)	IN625 mono-material		850 ± 30	1210 ± 30	38 ± 1
H_{xy}_Ni (CuCrZr)	CuCrZr mono-material		240 ± 10	290 ± 10	20 ± 7
H_{xz}_Cu	CuCrZr on IN625		430 ± 40	540 ± 90	15 ± 3
H_{xz}_Ni	IN625 on CuCrZr		490 ± 20	730 ± 40	28 ± 6
V_{xz}	IN625 | CuCrZr		270 ± 10	320 ± 10	13 ± 1
V_{xy}	IN625 | CuCrZr		263 ± 6	309 ± 7	16 ± 1

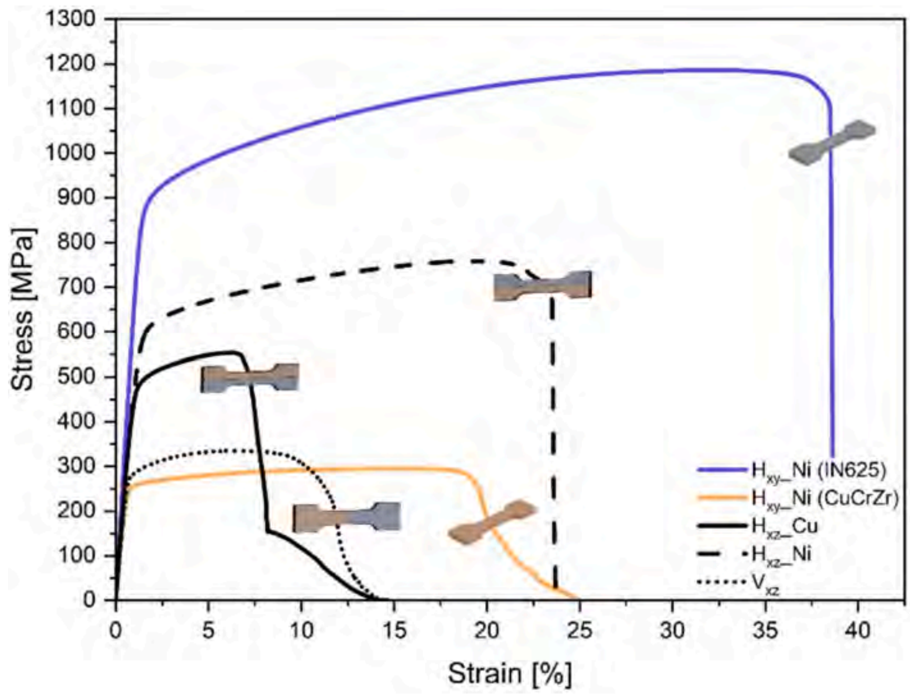

Fig. 7. Representative engineering stress–strain curves for the investigated specimens.

3.2. Mechanical response of the different joints

To link microstructure and mechanical response, uniaxial tensile tests were carried out on both mono- and bi-material samples according to the different interface configurations. Table 3 summarizes the measured tensile properties, while Fig. 7 reports representative stress-stain curves for each sample group. The complete set of stress–strain curves used for the determination of the values reported in Table 3 is provided in Fig. S3 of the Supplementary Information.

The mechanical properties of IN625 and CuCrZr mono-material specimens are consistent with literature data [38–40]. As expected, both strength and elongation of IN625 are higher than those of CuCrZr alloy with no significant differences related to the printing sequence of the bars from which the mono-material dog-bone specimens were extracted. A higher scatter in the obtained results is observed for the mono-material CuCrZr alloy. While all specimens show a comparable elastic and early plastic regions, those extracted from the same bar display markedly different elongations at fracture. This variability is attributed to the heterogeneous distribution of defects which promote non-uniform strain localization and premature crack initiation in some specimens.

The mechanical behavior of the bi-material specimens depends strongly on the loading scheme, i.e. whether the two materials are arranged in series (interface is perpendicular to the loading direction) or in parallel (interface parallel to the loading axis). In the serial-loading configuration, the applied strain is accommodated sequentially by the two materials, and the global response is therefore mainly governed by the weaker and more compliant CuCrZr region. Conversely, in the parallel-loading configuration, both materials are simultaneously subjected to the same macroscopic strain and the load is shared according to their relative stiffness, strength, and effective cross-sectional contribution. In this case, the mechanical response becomes more sensitive to interfacial bonding, strain compatibility between the two alloys, and defect distribution along the interface.

The former specimens, namely those with vertical interfaces (samples V_{xy} and V_{xz}), show that the softer CuCrZr alloy dominates the overall mechanical response, with limited differences related to the extraction direction and marginal effects on fracture elongation. Overall, the contribution of IN625 to the total ductility is markedly lower than that of CuCrZr, since IN625 remains largely in the elastic regime and does not reach its plastic yield point before joint failure. Nonetheless, fracture consistently occurs far from the interface, in the CuCrZr region, confirming the quality of the metallurgical bond region between the two alloys. These results are in agreement with literature results obtained on similar systems [18,20].

For specimens with interface parallel to the loading direction, namely those with horizontal interfaces (samples H_{xz}_Cu and H_{xz}_Ni), the engineering stress–strain curves reveal an intermediate behavior in terms of achieved yield and ultimate strength. With this configuration, the more resistant IN625 alloy sustains most of the applied load, while CuCrZr contributes marginally to the overall performance, behaving as a passive element. Consequently, the CuCrZr region leads to reduced global strength and ductility.

A clear dependence on the printing sequence on tensile properties is also observed. Specimens extracted from the IN625-on-CuCrZr bar (H_{xz}_Ni) exhibit superior mechanical properties compared to those cut out from the opposite configuration (H_{xz}_Cu), showing a 12 % increase in yield strength, a 26 % increase in UTS, and a 46 % increase in elongation at fracture. This systematic advantage reflects the observed differences in microstructure and defect distribution induced by the printing order of the materials, which govern fracture mechanisms. These findings highlight that the mechanical performance of multi-material systems is not solely dictated by the intrinsic properties of the constituent alloys but also by interface morphology, defect population, and processing strategy.

The lower mechanical performance of H_{xz}_Cu can therefore be related to the combined effect of a wider intermixing zone, higher defect density, and reduced interfacial cohesion. The extensive elemental mixing observed in this configuration promotes the formation of a crack-susceptible Cu–Ni transition region, where pores and microcracks are preferentially located and oriented normal to load direction. These defects act as local stress concentrators and facilitate strain localization and crack propagation normal to the interface. In contrast, the sharper and less defective interface of H_{xz}_Ni promotes more effective load transfer between the two materials, leading to higher strength and ductility. Although residual stresses were not directly measured in this work, they may also contribute to the observed behavior, particularly in H_{xz}_Cu, where the larger mixed region and the mismatch in thermo-physical properties between IN625 and CuCrZr can enhance local stress accumulation during cooling.

3.3. Fracture mechanism of the different joints

The fracture behavior is strongly affected by the relative strength of the interface with respect to the adjacent matrix regions. For the vertical-interface configuration, fracture consistently occurred within the CuCrZr region and far from the interface, indicating that the metallurgical bond between IN625 and CuCrZr is stronger than the CuCrZr matrix under serial loading. Therefore, in this configuration, the interface does not represent the preferential failure path and the overall fracture response is governed by the weaker CuCrZr region. Conversely, for the horizontal-interface configurations, the interface is parallel to the loading direction and its morphology has a more direct influence on crack propagation. In this case, the width of the intermixing zone and the local defect population determine whether the interface behaves as a cohesive load-transfer region or as a preferential crack path.

In the H_{xz}_Cu specimens (CuCrZr-on-IN625), crack initiation typically occurs at the interfacial region from cracks oriented perpendicular to the interface, where a high concentration of microcracks and pores is observed. These defects act as local stress concentrators and promote strain localization. Crack propagation first develops through the CuCrZr side and subsequently extends into the IN625 side (Fig. 8a). The failure of the IN625 portion causes the sharp stress drop observed in the engineering stress–strain curve (Fig. 7). This event precedes the final fracture of the specimen, which occurs only after the remaining, more ductile CuCrZr portion completely fails. The full video is available in Supplementary Video 1.

In contrast, in the H_{xz}_Ni specimens (IN625-on-CuCrZr), the interface is sharper and less defective, resulting in improved interfacial cohesion and more effective load transfer between the two alloys. Cracks originate from the external surfaces of the samples, predominantly within the CuCrZr region, which contains the highest concentration of defects, and grow inward until they reach the IN625 region, leading to final fracture with limited crack opening (Fig. 8b). The full video is available in Supplementary Video 2.

SEM fractographic analysis was conducted on the tensile-tested specimens, and representative images are reported in the Supplementary Information (Fig. S4). The mono-material IN625 and CuCrZr samples exhibit predominantly ductile fracture characterized by microvoid coalescence, in agreement with literature data for PBF-LB/M processed alloys [39,41], with particularly pronounced dimples in CuCrZr. The V_{xz} configuration failed within the CuCrZr region, sufficiently far from the interface, and its fracture morphology is fully consistent with that of the mono-material CuCrZr sample, further confirming that the interface is stronger than the CuCrZr matrix in the vertical configuration. Conversely, clear differences are observed at the interface for H_{xz}_Cu and H_{xz}_Ni. The H_{xz}_Cu specimen (Fig. S4a) shows planar facets and terrace-like features at the interface, indicating a brittle/quasi-cleavage contribution. These features are consistent with crack initiation from defects oriented perpendicular to the interface, likely promoted by the presence of interfacial cracks and pores within the broad transition zone. Crack propagation then proceeds first through the CuCrZr side and subsequently extends into the IN625 side. In contrast, H_{xz}_Ni (Fig. S4b) exhibits a rougher and more tortuous fracture morphology with evidence of ductile bridging, suggesting improved interfacial cohesion, more effective load transfer, and greater local plastic dissipation prior to failure.

These fracture features, including the observed crack initiation and propagation paths, are consistent with the combined EDS and EBSD results. In H_{xz}_Cu, the EDS profiles reveal the widest compositional transition, while EBSD shows an extended refined equiaxed-grain region, indicating extensive remelting and alloy mixing. This broad intermixing zone corresponds to the region where pores and micro-cracks are concentrated, providing a preferential crack path and explaining the lower strength and ductility of this configuration. Conversely, in H_{xz}_Ni, the sharper EDS transition and narrower refined region observed by EBSD indicate limited intermixing, which is consistent with the more cohesive fracture behavior, more effective load transfer, and higher tensile properties measured for this configuration.

Therefore, crack propagation is directly controlled by the local interface morphology. A narrow and less defective interface, as observed in H_{xz}_Ni, promotes cohesive load transfer between IN625 and CuCrZr. Conversely, a broad intermixing zone containing cracks and pores, as observed in H_{xz}_Cu, provides a preferential crack path and reduces the apparent joint strength and ductility.

3.4. Thermal diffusivity

Given that the IN625–CuCrZr combination targets applications demanding efficient heat dissipation along with mechanical strength, its thermal response was evaluated by LFA analyses. Room-temperature thermal diffusivities for mono- and multi-material specimens are reported in Fig. 9 and in Table S1 in the Supplementary Information. The thermal diffusivities measured for IN625 (0.028 cm^2/s) are consistent across configurations and align with literature data [21]. The diffusivity values obtained for CuCrZr are likewise of the same order of magnitude as those reported in previous studies [37,40], however, there is evidence of configuration-dependent variations in thermal diffusivity resulting from differences in thermal history. Specifically, the single-material CuCrZr sample extracted from H_Ni (IN625-on-CuCrZr) cubes exhibits

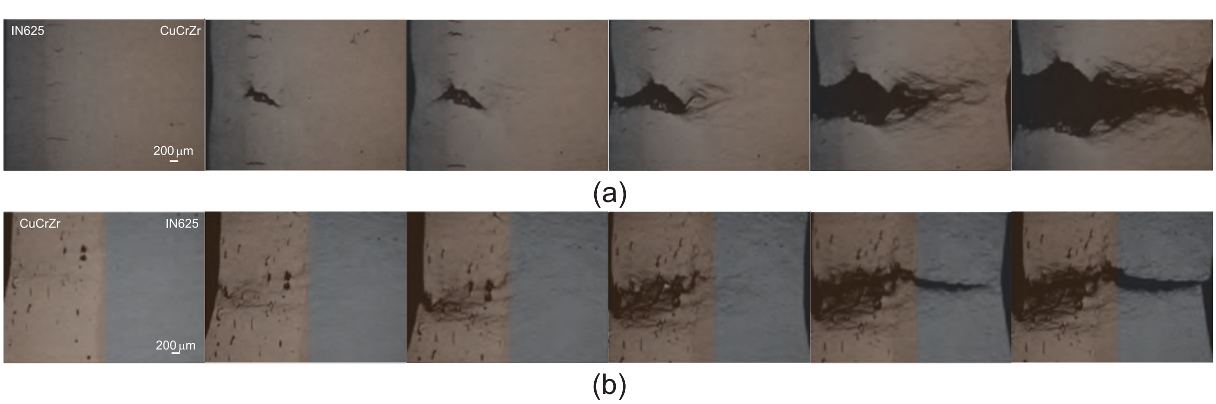

Fig. 8. SEM micrographs collected during *in-situ* tensile tests illustrating crack propagation for sample H_{xz}_Cu (a) and H_{xz}_Ni (b). Micrographs were artificially colored to distinguish the materials: CuCrZr (orange) and IN625 (gray). (For interpretation of the references to colour in this figure legend, the reader is referred to the web version of this article.)

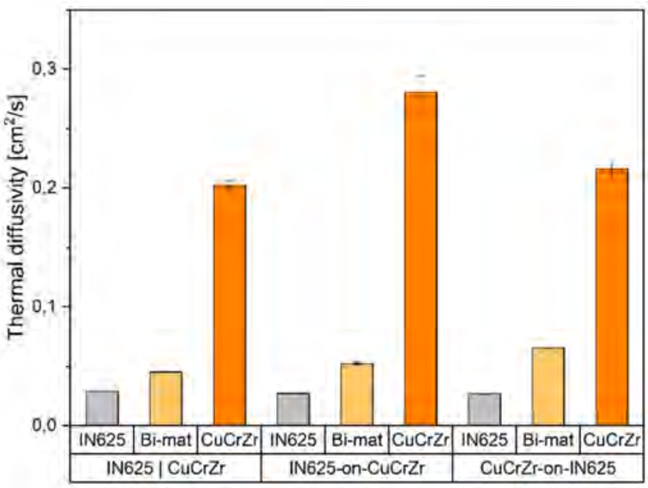

Fig. 9. Thermal diffusivity forIN625, bi-material specimen and CuCrZr alloy, extracted from the indicated sample.

the highest diffusivity (0.28 cm^2/s). This is consistent with the hypothesis that the *in-situ* thermal cycles induced by the subsequent layer deposition lead to incomplete aging, promoting secondary phase precipitation and reduction of solute content in the Cu matrix, resulting in higher thermal diffusivity.

Mono-material samples extracted from V_{yz} specimen shows the lowest diffusivity (0.20 cm^2/s). In this case, solute depletion within the matrix is localized only in half of the specimen, and diffusivity is further reduced by the higher porosity observed in the bulk Cu region. Grain orientation may also play a role on thermal diffusivity. In V_{yz}, columnar grains are aligned perpendicular to the measurement direction, introducing anisotropy in heat transfer.

For the multi-material samples, measurements were performed on specimens exhibiting a comparable average Cu content (52 $\pm$ 3 wt%). In all cases, diffusivity values exceed those of IN625, with gains up to 145 % in H_{xy}_Cu. This result indicates that, within the investigated configurations, the IN625–CuCrZr interface does not act as a thermal barrier and does not hinder the effective heat transfer across the multi-material specimens. Interestingly, the highest diffusivity is obtained for the configuration characterized by the broadest and most defective intermixing region. This suggests that, within the present dataset local defectivity is not the dominant factor controlling thermal diffusivity. Rather, the effective thermal response appears to be associated with the spatial distribution and continuity of Cu-rich/CuCrZr-like regions along the heat-flow direction and this is related to the width of the transition zone. Secondary factors such as local composition gradients, grain size and orientation, porosity, precipitation state, and interfacial mixing may also contribute to the measured values; however, their individual effects cannot be quantitatively separated with the present experimental dataset.

4. Conclusions

This study assessed the microstructural, mechanical and thermal behavior of IN625–CuCrZr multi-materials fabricated via PBF-LB/M featuring three different interface configurations.

Microstructural and compositional analyses revealed that the width of the interfacial region varied markedly with interface type and deposition sequence, ranging from nearly 2 mm to approximately 350 μm, following the trend CuCrZr-on-IN625 > IN625 | CuCrZr > IN625-on-CuCrZr. In all configurations, the transition zone extended predominantly into the CuCrZr domain and exhibited extremely fine, equiaxed grains. Cracks, mainly intergranular and propagating along IN625 grain boundaries, were detected within the Cu–Ni mixed region of the CuCrZr-on-IN625 samples, where Cu-rich films between Ni-rich grains formed due to liquid-phase separation. These features indicate that extensive alloy mixing during processing promotes interfacial cracking within the critical 20–40 wt% Cu range.

Mechanical tests on miniaturized specimens containing the different interface configurations showed that under loading parallel to the interface, horizontal IN625-on-CuCrZr specimens achieved the highest tensile strength (730 MPa), whereas the CuCrZr-on-IN625 configuration reached 540 MPa. Fracture mechanisms were fully consistent with the microstructural findings: in the IN625-on-CuCrZr sample, cracks initiated in the defect-rich Cu side and propagated into the Ni matrix, while in the CuCrZr-on-IN625 sample, interfacial cracks led to premature failure of the IN625 region. Vertical interfaces exhibited lower strength (320 MPa), with fracture occurring mostly within the bulk CuCrZr rather than at the interface.

Thermal diffusivity measurements revealed an enhancement of the effective thermal response in all multi-material samples compared with IN625, driven by the high intrinsic conductivity of the CuCrZr region. The results indicate that the IN625–CuCrZr interface does not appear to act as a significant thermal barrier under the investigated conditions. Variations among configurations are likely associated with the spatial distribution and continuity of Cu-rich/CuCrZr-like regions along the heat-flow direction, while secondary effects such as interfacial morphology, alloy mixing, porosity, texture, and possible aging may also contribute.

Overall, these findings highlight the critical role of interface morphology and composition in governing the mechanical strength and integrity of PBF-LB/M IN625–CuCrZr multi-materials. In particular, the results indicate that deposition strategies promoting sharper compositional transitions can mitigate cracking by limiting the formation of compositions within the critical Cu range, although excessive interface sharpness may also induce local stress concentrations. These observations provide experimentally supported design considerations for selecting deposition sequence and interface architecture in IN625–CuCrZr multi-material components.

CRediT authorship contribution statement

Silvia Marola: Writing – original draft, Visualization, Validation, Supervision, Methodology, Investigation, Formal analysis, Data curation, Conceptualization. **Alessandro Carella:** Writing – review & editing, Visualization, Investigation, Formal analysis, Data curation. **Riccardo Casati:** Writing – review & editing, Supervision, Project administration, Funding acquisition. **Maurizio Vedani:** Writing – review & editing, Supervision, Project administration, Funding acquisition.

Funding

This study was partially funded by MICS (Made in Italy – Circular and Sustainable) Extended Partnership and received funding from the European Union Next-Generation EU (PIANO NAZIONALE DI RIPRESA E RESILIENZA (PNRR) – MISSIONE 4 COMPONENTE 2, INVESTIMENTO 1.3 – D.D. 1551.11-10-2022, PE00000004).

Declaration of competing interest

The authors declare the following financial interests/personal relationships which may be considered as potential competing interests: [Riccardo Casati reports financial support was provided by European Commission. If there are other authors, they declare that they have no known competing financial interests or personal relationships that could have appeared to influence the work reported in this paper.].

Appendix A. Supplementary data

Supplementary data to this article can be found online at https://doi.org/10.1016/j.matdes.2026.116443.

Data availability

Data will be made available on request.

References

[1] M. Manjaiah, K. Raghavendra, N. Balashanmugam, J. Paulo Davim, eds., Additive Manufacturing, Elsevier, 2021, doi: 10.1016/C2019-0-04429-9.
[2] T. DebRoy, H.L.L. Wei, J.S.S. Zuback, T. Mukherjee, J.W.W. Elmer, J.O. O. Milewski, A.M.M. Beese, A. Wilson-Heid, A. De, W. Zhang, Additive manufacturing of metallic components – process, structure and properties, Prog. Mater Sci. 92 (2018) 112–224, https://doi.org/10.1016/j.pmatsci.2017.10.001.
[3] T. Romano, M. Abdelwahed, V. Bertolo, T. Cecotti, S. Skhosane, G. Mahadevan, V. Popovich, M. Hermans, M.A. Taha, S. Pityana, M. Vedani, Microstructural, mechanical, and thermal characterization of constitutive layers in copper-steel functionally graded material manufactured via laser directed energy deposition, Mater. Des. 256 (2025) 114329, https://doi.org/10.1016/j.matdes.2025.114329.
[4] O.M. Al-Jamal, S. Hinduja, L. Li, Characteristics of the bond in Cu–H13 tool steel parts fabricated using SLM, CIRP Ann. 57 (2008) 239–242, https://doi.org/10.1016/j.cirp.2008.03.010.
[5] C. Wei, Z. Sun, Q. Chen, Z. Liu, L. Li, Additive manufacturing of horizontal and 3D functionally graded 316L/Cu10Sn components via multiple material selective laser melting, J. Manuf. Sci. Eng. 141 (2019), https://doi.org/10.1115/1.4043983.
[6] L. Liu, D. Wang, C. Han, Y. Li, T. Wang, Y. Wei, W. Zhou, M. Yan, Y. Liu, S. Wei, Y. Yang, Additive manufacturing of multi-materials with interfacial component gradient by in-situ powder mixing and laser powder bed fusion, J. Alloys Compd. 978 (2024) 173508, https://doi.org/10.1016/j.jallcom.2024.173508.
[7] A. Nazir, O. Gokcekaya, K. Md Masum Billah, O. Ertugrul, J. Jiang, J. Sun, S. Hussain, Multi-material additive manufacturing: a systematic review of design, properties, applications, challenges, and 3D printing of materials and cellular metamaterials, Mater. Des. 226 (2023), https://doi.org/10.1016/j.matdes.2023.111661.
[8] A. Bandyopadhyay, Y. Zhang, B. Onuike, Additive manufacturing of bimetallic structures, Virtual Phys. Prototyp. 17 (2022) 256–294, https://doi.org/10.1080/17452759.2022.2040738.
[9] C.P. Martendal, P.D.B. Esteves, L. Deillon, F. Malamud, A.M. Jamili, J.F. Löffler, M. Bambach, Effects of beam shaping on copper-steel interfaces in multi-material laser beam powder bed fusion, J. Mater. Process. Technol. 327 (2024) 118344, https://doi.org/10.1016/j.jmatprotec.2024.118344.
[10] R. Anderson, J. Terrell, J. Schneider, S. Thompson, P. Gradl, Characteristics of Bi-metallic interfaces formed during direct energy deposition additive manufacturing processing, Metall. Mater. Trans. B 50 (2019) 1921–1930, https://doi.org/10.1007/s11663-019-01612-1.
[11] B. Neirinck, X. Li, M. Hick, Powder deposition systems used in powder bed-based multimetal additive manufacturing, Acc. Mater. Res. 2 (2021) 387–393, https://doi.org/10.1021/accountsmr.1c00030.
[12] A. Mussatto, Research progress in multi-material laser-powder bed fusion additive manufacturing: a review of the state-of-the-art techniques for depositing multiple powders with spatial selectivity in a single layer, Results Eng. 16 (2022), https://doi.org/10.1016/j.rineng.2022.100769.
[13] A. Bulloch, A. Harris, A. Groom, A. Cruchley, C.J. Tuck, M. Simonelli, Fundamental investigation of the interface formation of multi-material additive manufactured 316L-CuSn10 structures, Metall. Mater. Trans. A Phys. Metall. Mater. Sci. 56 (2025) 2586–2603, https://doi.org/10.1007/s11661-025-07817-1.
[14] B. Li, C. Han, C.W.J. Lim, K. Zhou, Interface formation and deformation behaviors of an additively manufactured nickel-aluminum-bronze/15-5 PH multimaterial via laser-powder directed energy deposition, Mater. Sci. Eng. A 829 (2022) 142101, https://doi.org/10.1016/j.msea.2021.142101.
[15] Z.H. Liu, D.Q. Zhang, S.L. Sing, C.K. Chua, L.E. Loh, Interfacial characterization of SLM parts in multi-material processing: Metallurgical diffusion between 316L stainless steel and C18400 copper alloy, Mater Charact 94 (2014) 116–125, https://doi.org/10.1016/j.matchar.2014.05.001.
[16] W. Zhang, H. Liao, Z. Hu, S. Zhang, B. Chen, H. Yang, Y. Wang, H. Zhu, Interfacial characteristics and mechanical properties of additive manufacturing martensite stainless steel on the Cu-Cr alloy substrate by directed energy deposition, J. Mater. Sci. Technol. 90 (2021) 121–132, https://doi.org/10.1016/j.jmst.2021.03.008.
[17] A. Marques, Â. Cunha, M. Gasik, O. Carvalho, F.S. Silva, F. Bartolomeu, Inconel 718–copper parts fabricated by 3D multi-material laser powder bed fusion: a novel technological and designing approach for rocket engine, Int. J. Adv. Manuf. Technol. 122 (2022) 2113–2123, https://doi.org/10.1007/s00170-022-10011-x.
[18] P.R. Gradl, T.W. Teasley, C.S. Protz, M.B. Garcia, D. Ellis, C. Kantzos, Advancing GRCop-based Bimetallic Additive Manufacturing to Optimize Component Design and Applications for Liquid Rocket Engines, in: AIAA Propulsion and Energy 2021 Forum, American Institute of Aeronautics and Astronautics, Reston, Virginia, 2021, doi: 10.2514/6.2021-3231.
[19] A. Baganis, F. Malamud, J. Čapek, F.F. Klimashin, E. Polatidis, M. Busi, M. Šmíd, M. Jambor, J. Michler, M. Strobl, C. Leinenbach, Phase formation and texture evolution in 316L-CuCrZr multi-material structures fabricated by laser powder bed fusion, Mater. Des. 256 (2025), https://doi.org/10.1016/j.matdes.2025.114358.
[20] R. Zhao, L. Li, Z. Nie, Z. Ma, Q. Guo, Effects of pre-heating induced interfacial diffusion on microstructure and related mechanical properties of direct laser metal deposited Inconel 625 superalloy on a Cu-Cr-Zr substrate, Mater. Sci. Eng. A 920 (2025) 147551, https://doi.org/10.1016/j.msea.2024.147551.
[21] T. Pan, X. Zhang, T. Yamazaki, A. Sutton, W. Cui, L. Li, F. Liou, Characteristics of Inconel 625—copper bimetallic structure fabricated by directed energy deposition, Int. J. Adv. Manuf. Technol. 109 (2020) 1261–1274, https://doi.org/10.1007/s00170-020-05713-z.
[22] J. Preis, Z. Wang, J. Howard, Y. Lu, N. Wannenmacher, S. Shen, B.K. Paul, S. Pasebani, Effect of laser power and deposition sequence on microstructure of GRCop42 - Inconel 625 joints fabricated using laser directed energy deposition, Mater. Des. 241 (2024), https://doi.org/10.1016/j.matdes.2024.112944.
[23] T.B. Massalski, J.L. Murray, L.H. Bennett, H. Baker, eds., Binary alloy phase diagrams, Metals Park, OH: American society for metals, 1986.
[24] A. Özsoy, S. Gaudez, W.A. Hearn, A. Baganis, Z. Hegedüs, Y. Chen, A. Rack, R. E. Logé, S. Van Petegem, Phase-separation-driven cracking in additive manufacturing of Ni-Cu alloy systems, Addit. Manuf. 110 (2025), https://doi.org/10.1016/j.addma.2025.104950.
[25] D. Gu, X. Shi, R. Poprawe, D.L. Bourell, R. Setchi, J. Zhu, Material-structure-performance integrated laser-metal additive manufacturing, Science (1979). 372 (2021), doi: 10.1126/science.abg1487.
[26] I. Meyer, M. Oel, T. Ehlers, R. Lachmayer, Additive manufacturing of multi-material parts – design guidelines for manufacturing of 316L/CuCrZr in laser powder bed fusion, Heliyon 9 (2023), https://doi.org/10.1016/j.heliyon.2023.e18301.
[27] S. N. Samad, J. Griffis, G. Manogharan, N. Kouraytem, Multi-material additive manufacturing of metals: A review of structures and mechanical characteristics, Eng. Sci. Additive Manuf., 1 (2025) 025180010, doi: 10.36922/ESAM025180010.
[28] A. El Hassanin, F. Scherillo, U. Prisco, R. Sansone, A. Astarita, Selective laser melting of Cu-inconel 718 powder mixtures, J. Manuf. Process. 59 (2020) 679–689, https://doi.org/10.1016/j.jmapro.2020.10.039.
[29] B. Onuike, B. Heer, A. Bandyopadhyay, Additive manufacturing of Inconel 718—Copper alloy bimetallic structure using laser engineered net shaping (LENS^{TM}), Addit. Manuf. 21 (2018) 133–140, https://doi.org/10.1016/j.addma.2018.02.007.
[30] S. Moriya, T. Inoue, M. Sasaki, T. Nakamoto, T. Kimura, N. Nomura, K. Kikuchi, A. Kawasaki, T. Kato, I. Masuda, Feasibility study on additive manufacturing of liquid rocket combustion chamber, transactions of the japan society for aeronautical and space sciences, Aerospace Technology Japan 16 (2018) 261–266, https://doi.org/10.2322/tastj.16.261.
[31] G.-S. Zou, X. Yang, D.-X. Cheng, H. Gu, M.-N. Zhang, J.-Y. Xu, C. Wei, J.-H. Yao, L. Li, Interface characterization and mechanical properties of laser powder bed fused IN718-CuSn10 functionally gradient materials, Mater. Today Commun. 45 (2025) 112411, https://doi.org/10.1016/j.mtcomm.2025.112411.
[32] L. Zhang, P. Dong, Y. Zeng, H. Yao, J. Chen, Additive manufacturing of Inconel 718/CuCrZr multi-metallic materials fabricated by laser powder bed fusion, Addit. Manuf. 92 (2024) 104377, https://doi.org/10.1016/j.addma.2024.104377.
[33] L. Liu, D. Wang, T. Wang, C. Han, Y. Li, H. Tan, W. Zhou, X. Yan, L. Lei, Y. Yang, Laser additive manufacturing of multimaterials with hierarchical interlocking interface via a flexible scraper-based method, Int. J. Mach. Tools Manuf 205 (2025), https://doi.org/10.1016/j.ijmachtools.2024.104236.
[34] W.H. Kan, L.N.S. Chiu, C.V.S. Lim, Y. Zhu, Y. Tian, D. Jiang, A. Huang, A critical review on the effects of process-induced porosity on the mechanical properties of alloys fabricated by laser powder bed fusion, J. Mater. Sci. 57 (2022) 9818–9865, https://doi.org/10.1007/s10853-022-06990-7.
[35] K. Dongfang, H. Fan, S. Sui, H. Li, H. Liu, Y. Li, P. Liu, Effect of laser powder bed fusion process parameters on the microstructures, mechanical properties, and conductivity of CuCrZr alloy, J. Mater. Eng. Perform. 34 (2025) 13304–13317, https://doi.org/10.1007/s11665-024-10026-3.
[36] T. Keya, R.D. Fischer, M. Andurkar, S.M. Thompson, V. O'Donnell, J. Gahl, B. C. Prorok, Evolution of precipitates and microhardness of L-PBF inconel 625 through relevant thermal treatment, Alloys 3 (2024) 295–312, https://doi.org/10.3390/alloys3040018.
[37] X. Tang, X. Chen, F. Sun, L. Li, P. Liu, H. Zhou, S. Fu, A. Li, A study on the mechanical and electrical properties of high-strength CuCrZr alloy fabricated using laser powder bed fusion, J. Alloys Compd. 924 (2022), https://doi.org/10.1016/j.jallcom.2022.166627.
[38] M. Karmuhilan, S. Kumanan, A review on additive manufacturing processes of inconel 625, J. Mater. Eng. Perform. 31 (2022) 2583–2592, https://doi.org/10.1007/s11665-021-06427-3.
[39] J. Zhou, Y. Huang, Z. Li, X. Tong, D. You, J. Yang, Q. Zhang, W. Li, X. Wang, Effect of heat treatments on microstructure, mechanical and electrical properties of Cu–Cr–Zr alloy manufactured by laser powder bed fusion, Mater. Chem. Phys. 296 (2023) 127249, https://doi.org/10.1016/j.matchemphys.2022.127249.
[40] C. Wallis, B. Buchmayr, Effect of heat treatments on microstructure and properties of CuCrZr produced by laser-powder bed fusion, Mater. Sci. Eng. A 744 (2019) 215–223, https://doi.org/10.1016/j.msea.2018.12.017.
[41] K. Li, Y. Ren, G. Xie, J. He, Q. Chen, M. Zhang, D.Z. Zhang, H. Cao, L.E. Murr, Effect of solid-solution treatment on high-temperature properties and creep fracture mechanism of laser powder bed fused Inconel 625 alloy, Mater. Sci. Eng. A 902 (2024), https://doi.org/10.1016/j.msea.2024.146592.